

Review

Challenges Facing Pressure Retarded Osmosis Commercialization: A Short Review

Bassel A. Abdelkader  and Mostafa H. Sharqawy * 

School of Engineering, University of Guelph, Guelph, ON N1G 2W1, Canada

* Correspondence: melsharq@uoguelph.ca; Tel.: +1-(519)-824-4120 (ext. 58973)

Abstract: Pressure-retarded osmosis (PRO) is a promising technology that harvests salinity gradient energy. Even though PRO has great power-generating potential, its commercialization is currently facing many challenges. In this regard, this review highlights the discrepancies between the reported power density obtained by lab-scale PRO systems, as well as numerical investigations, and the significantly low power density values obtained by PRO pilot plants. This difference in performance is mainly due to the effect of a pressure drop and the draw pressure effect on the feed channel hydrodynamics, which have significant impacts on large-scale modules; however, it has a minor or no effect on small-scale ones. Therefore, this review outlines the underlying causes of the high power density values obtained by lab-scale PRO systems and numerical studies. Moreover, other challenges impeding PRO commercialization are discussed, including the effect of concentration polarization, the solution temperature, the pressure drop, and the draw pressure effect on the feed channel hydrodynamics. In conclusion, this review sheds valuable insights on the issues facing PRO commercialization and suggests recommendations that can facilitate the successful development of PRO power plants.

Keywords: pressure retarded osmosis; review; osmotic power challenges; PRO modules



Citation: Abdelkader, B.A.;

Sharqawy, M.H. Challenges Facing Pressure Retarded Osmosis

Commercialization: A Short Review. *Energies* **2022**, *15*, 7325. <https://doi.org/10.3390/en15197325>

Academic Editor: Marco Marengo

Received: 29 August 2022

Accepted: 29 September 2022

Published: 5 October 2022

Publisher's Note: MDPI stays neutral with regard to jurisdictional claims in published maps and institutional affiliations.



Copyright: © 2022 by the authors. Licensee MDPI, Basel, Switzerland. This article is an open access article distributed under the terms and conditions of the Creative Commons Attribution (CC BY) license (<https://creativecommons.org/licenses/by/4.0/>).

1. Introduction

Salinity gradient energy (SGE) is a promising form of renewable energy that provides clean sustainable energy and recently emerged as an alternative to fossil fuel power plants. SGE is generated from the salinity difference between two solutions, such as freshwater and seawater. SGE was first introduced by Pattle [1] as the energy available through the mixing of seawater and freshwater, where the energy generated depends on the osmotic pressure difference between the two solutions. There are several processes that utilize SGE to produce power, such as reverse electrodialysis (RED), pressure-retarded osmosis (PRO), capacitive mixing (CAPMIX), and reverse vapor compression (RVC) [2]. RED utilizes the electrochemical potential difference between the solutions through the directional flow of ions across ion-exchange membranes, generating power that is captured by electrodes [3]. PRO utilizes the osmotic pressure difference between two different salinity solutions across a semipermeable membrane to generate power [4]. CAPMIX, on the other hand, does not involve the use of membranes but uses porous electrodes submerged in an electrolyte to generate power from the chemical potential energy [5]. Similar to CAPMIX, RVC does not involve the use of membranes but generates power by utilizing the difference in vapor pressure between freshwater and seawater [6].

The performance of any SGE process can be assessed by determining its efficiency and power density. The efficiency indicates the amount of useful work produced relative to the available energy, which is the Gibbs free energy of mixing the two solutions. The power density is defined as the power produced per membrane surface area for PRO and RED, or per unit electrode mass in the case of CAPMIX. PRO has a higher power density when compared with RED and CAPMIX [7,8]. In addition, PRO has a higher efficiency range

(54–56%) compared with RED (18–38%), as reported by Yip and Elimelech [9]. Thus, PRO has a greater potential for power generation compared with other SGE technologies.

Compared with other forms of renewable energy technologies, PRO has a higher availability factor, as it is able to generate a constant power supply for base loads [10–16]. In addition, PRO has a higher energy conversion efficiency compared with other renewable energy technologies, such as those generating solar, geothermal, and wind energies [17]. The energy conversion efficiency is the ratio between the energy generated and the energy that is input or available. In the case of PRO, this efficiency is the ratio between the energy produced and the Gibbs free energy of mixing. The global power generation potential of PRO is estimated to be around 157 GW after considering losses and inefficiencies when using only 10% of the global rivers' water discharge [18]. This estimate can cover the energy demand of around half a billion people according to the average worldwide electricity consumption [18].

PRO is an osmotically driven process that utilizes the osmotic pressure difference between low- and high-salinity solutions, which was first described and patented by Leob [19] in 1975. Figure 1 shows a schematic of the basic components and the flow of solutions in the PRO process. In PRO, a semi-permeable membrane fixed in a membrane module separates the two solutions of different salt concentrations. The high-salinity solution (draw solution) is pressurized to a high pressure that is still lower than the osmotic pressure, while the low-salinity solution (feed solution) flows at a low pressure that overcomes the pressure drop in the module flow channel. The osmotic pressure difference between the two solutions drives water from the feed solution to the draw solution across the membrane [20,21]. The flow of water through the membrane dilutes the draw solution and increases its volume flow rate. A hydro turbine is then utilized to depressurize the high-pressure draw solution to generate energy that feeds the high-pressure pump and provides net positive power. The power generated by PRO is directly related to the amount of water permeated through the membrane from the feed solution to the draw solution, which depends on the osmotic pressure difference, as well as the membrane characteristics and operating conditions.

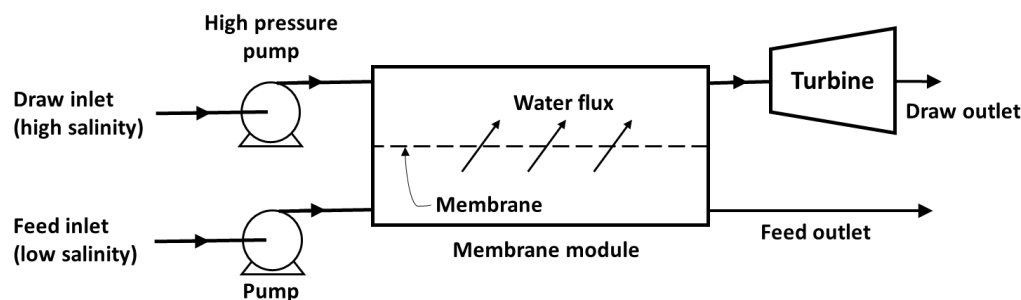


Figure 1. Schematic of a basic PRO process.

The high- and low-salinity solutions for PRO plants are available from various natural and industrial sources. The feed and draw solutions could be from freshwater and seawater present at river mouths, seawater, and brine rejected from desalination plants, or freshwater and wastewater rejected from water treatment plants [21,22]. As the concentration difference between the feed and draw solutions increases, the power generated increases significantly [23,24]. It was reported that the PRO power density increased by 6.5 times as the draw solution concentration increased from 0.5 M NaCl (i.e., 0.5 mol/liter NaCl solution, which is close to seawater salinity) to 1 M NaCl (similar to the salinity of rejected brine from a seawater reverse osmosis (RO) desalination plant), and 17.5 times as the draw concentration increased to 2 M NaCl (similar to brine rejected from a seawater FO desalination plant) with a feed concentration of 0.05 M NaCl [25]. However, at a higher feed solution concentration, the power density is significantly lower at the same concentration

difference between the feed and draw solutions due to the severe internal concentration polarization [25], as discussed later.

Despite its great potential, the commercialization of PRO faces several issues that limit its use for large-scale power production. One of the main challenges is the inefficiency of the commercially available membrane module and spacers for use in PRO [26–30]. The current spacers were reported to cause channel blockage and severe membrane deformation, increasing the pressure drop, and hence, reducing the PRO performance [29,30]. Moreover, the PRO performance is greatly reduced by the effect of the concentration polarization, which can either be internal, occurring inside the membrane support layer, or external, occurring near the membrane surface [21,31]. Another challenge limiting PRO performance is the occurrence of fouling, which is more significant when high-salinity solutions, such as seawater or wastewater, are used as the feed solution [32–34]. Moreover, the temperatures of the draw and feed solutions can significantly influence the PRO performance [35]. The solution temperatures depend on the geographical location and seasonal temperature fluctuations, as seawater temperatures can fluctuate from -2 to 35 °C throughout the year [36].

This review aimed to enhance the understanding of the challenges facing PRO commercialization. It starts with a discussion of the solution diffusion model, along with a comparison between the water flux predictions estimated using the different modified versions of the model. This is followed by a comprehensive comparison of the performance of plate-and-frame and spiral wound modules using commercially available membranes. This comparison surveys the experimental and numerical data of the performance of both modules available in the literature. A detailed discussion of the challenges facing PRO commercialization is then included, some of which were encountered and reported by the first PRO pilot plant. Finally, this review offers recommendations and insights on the future research required to achieve successful PRO commercialization.

2. Modeling of PRO Process

2.1. Osmotic Processes

Osmosis can be described as the spontaneous flow of water (or solvent) from a solution of high water potential (low salinity) to a solution of low water potential (high salinity) across a semipermeable membrane. There are three basic osmotic processes with different water flow directions that depend on both the osmotic and applied hydraulic pressure difference, namely, forward osmosis (FO), reverse osmosis (RO), and PRO. In an FO process, there is no hydraulic pressure difference applied and hence the water flux is generated by the osmotic pressure difference only from the low-salinity solution to the high-salinity solution. In PRO, the hydraulic pressure difference applied to the high-salinity solution is lower than the osmotic pressure difference, and hence, water will still flow from the low-salinity to the high-salinity solution, similar to the FO process. In RO, the hydraulic pressure difference applied is higher than the osmotic pressure difference and water flows in the opposite direction (i.e., from the high-salinity to the low-salinity solution). The flux reversal point is theoretically defined as the point at which the hydraulic pressure difference is equal to the osmotic pressure difference. In reality, the flux reversal point occurs at a hydraulic pressure difference that is lower than the osmotic pressure, as shown in Figure 2, due to the combined effects of the concentration polarization, draw solution dilution, and pressure drop. The PRO performance is assessed in terms of the power density, which is defined as the power generated per unit membrane area. Theoretically, the maximum power density occurs at the point at which the hydraulic pressure difference is equal to half the osmotic pressure difference. However, similar to the flux reversal point, the maximum power density is achieved at a lower hydraulic pressure difference, as shown in Figure 2.

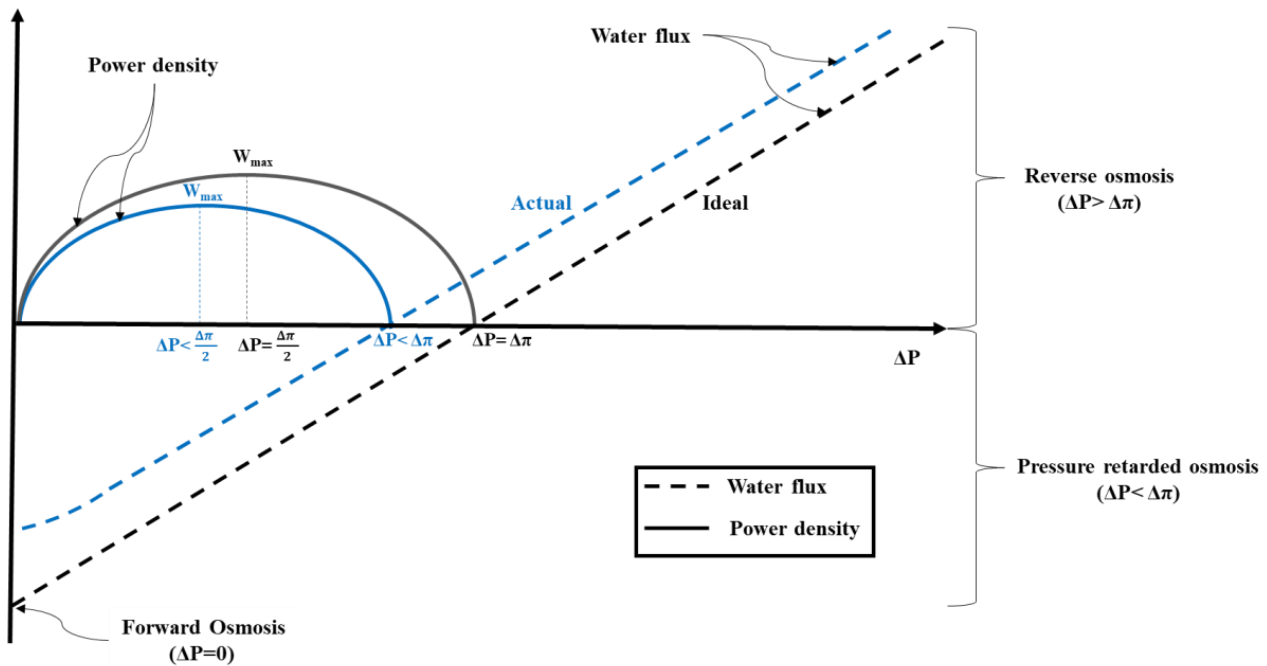


Figure 2. Variations in water flux with hydraulic pressure difference for FO, RO, and PRO processes, as well as changes in power density for PRO.

2.2. Solution Diffusion Model

2.2.1. Neglecting the Effect of Concentration Polarization

The water flux across a semipermeable membrane is defined by the following equation:

$$J_w = A(\Delta\pi - \Delta P) \tag{1}$$

where A is the water permeability coefficient, $\Delta\pi$ is the osmotic pressure difference, and ΔP is the hydraulic pressure difference. The PRO performance is assessed through the power density W , which is the power generated per membrane surface area and is given by

$$W = J_w \Delta P = A(\Delta\pi - \Delta P)\Delta P \tag{2}$$

To find the optimal ΔP that achieves a maximum power density, Equation (2) should be differentiated with respect to ΔP . The maximum power density occurs at $\Delta P = \Delta\pi/2$, yielding the following expression for the theoretical maximum power density:

$$W_{max} = A \frac{\Delta\pi^2}{4} \tag{3}$$

In this theoretical maximum power density expression, the effects of the concentration polarization and salt flux across the membrane are neglected. In real membranes, the concentration polarization reduces the osmotic pressure difference and subsequently lowers the water flux reversal point. In addition, the salt flux across the membrane changes both feed and draw solution concentrations along the membrane length, reducing the osmotic pressure difference. Therefore, the combined effects of the concentration polarization and salt flux in real membranes will result in the maximum power density occurring at a lower pressure difference compared with the theoretical maximum power density, i.e., $\Delta P < \Delta\pi/2$.

2.2.2. Lee’s Model

In 1981, Lee et al. [37] considered the effect of internal concentration polarization (ICP) in the solution diffusion model but ignored the effect of the external concentration polariza-

tion (ECP). Referring to Figure 3, they neglected the ECP by assuming that $C_{D,b} = C_{D,m}$ and $C_{F,b} = C_{F,m}$. This assumption is valid if there is a high degree of turbulence near the membrane surface. Therefore, they modified the osmotic pressure difference in Equation (1), yielding the following expression:

$$J_w = A(\Delta\pi_{eff} - \Delta P) = A(\pi_{D,m} - \pi_{icp} - \Delta P) \quad (4)$$

where $\Delta\pi_{eff}$ is the effective osmotic pressure difference between the active layer membrane surface ($\pi_{D,m}$) and the active–support layer interface (π_{icp}), as shown in Figure 3. Using van't Hoff's model, the osmotic pressure as a function of the concentration is given as

$$\pi = \beta RTC \quad (5)$$

where β is the van't Hoff coefficient, R_u is the universal gas constant, T is the absolute temperature, and C is the salt concentration.

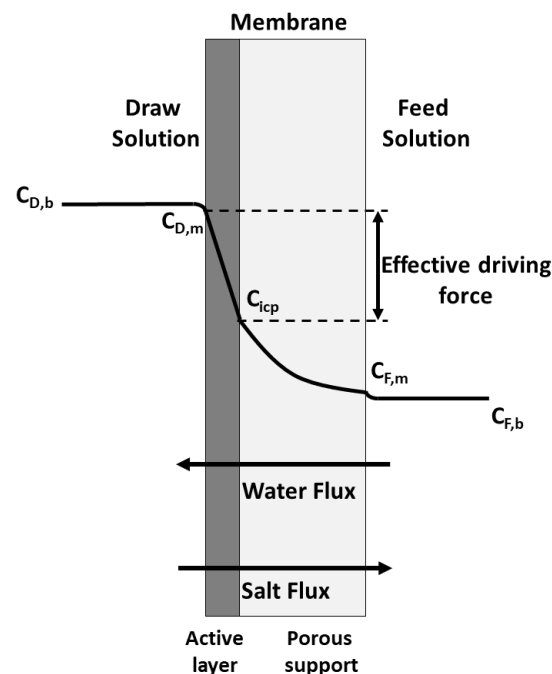


Figure 3. PRO concentration profile for an asymmetric membrane with the active dense layer facing the draw solution.

The salt (or solute) flux across the membrane active layer is defined by Equation (6):

$$J_s = B(C_{D,m} - C_{icp}) \quad (6)$$

where B is the salt permeability coefficient, $C_{D,m}$ is the concentration at the active layer, and C_{icp} is the concentration at the active–support layer interface.

The mass transport of the salt across the membrane support layer is caused by diffusion due to the presence of the salt gradient and convection due to water flux across the membrane. The effect of diffusion is represented by the first term in Equation (7), while the second term represents the convection effect:

$$J_s = D\varepsilon \frac{dC(x)}{dx} - J_w C(x) \quad (7)$$

where D is the diffusion coefficient in the membrane support layer and ε is the porosity of the membrane support layer. Rearrangement of Equation (7) gives

$$\frac{1}{C(x) + \frac{J_s}{J_w}} dC(x) = \frac{J_w}{D\varepsilon} dx \quad (8)$$

Integrating Equation (8) using the boundary conditions $C(x) = C_{F,m}$ at $x = 0$ and $C(x) = C_{icp}$ at $x = \tau t$, where x is the distance measured from the membrane support layer toward the membrane active layer, yields the following expression:

$$C_{icp} = C_{F,m} \exp\left(J_w \frac{\tau t}{D\varepsilon}\right) + \frac{J_s}{J_w} \left[\exp\left(J_w \frac{\tau t}{D\varepsilon}\right) - 1 \right] \quad (9)$$

where t represents the thickness of the membrane support layer and τ is the tortuosity of the membrane support layer. Substituting Equation (6) into Equation (9) yields the following equation:

$$C_{icp} = \frac{B[\exp(J_w K) - 1](C_{D,m} - C_{icp})}{J_w} + C_{F,m} \exp(J_w K) \quad (10)$$

where K is the solute resistivity for diffusion inside the support layer, as given by Equation (11):

$$K = \frac{\tau t}{D\varepsilon} = \frac{S}{D} \quad (11)$$

where S is the membrane structure parameter.

Rearranging Equation (10) and Equation (4) gives

$$\frac{C_{icp}}{C_{D,m}} = \frac{B[\exp(J_w K) - 1] + J_w \frac{C_{F,m}}{C_{D,m}} \exp(J_w K)}{B[\exp(J_w K) - 1] + J_w} \quad (12)$$

$$J_w = A \left(\pi_{D,m} \left(1 - \frac{\pi_{icp}}{\pi_{D,m}} \right) - \Delta P \right) \quad (13)$$

Using van't Hoff's equation (Equation (5)), the ratio of the salt concentrations can be assumed to be equal to the ratio of the osmotic pressure (i.e., $\frac{\pi_{icp}}{\pi_{D,m}} = \frac{C_{icp}}{C_{D,m}}$). Using this assumption, Equations (13) and (12) can be combined to yield the following expression for the water flux:

$$J_w = A \left(\pi_{D,m} \frac{1 - \frac{C_{F,m}}{C_{D,m}} \exp(J_w K)}{1 + \frac{B}{J_w} [\exp(J_w K) - 1]} - \Delta P \right) \quad (14)$$

As the effect of the external concentration polarization is neglected, the concentrations at the membrane surface can be replaced with the bulk low concentrations, i.e., $C_{D,b} = C_{D,m}$ and $C_{F,b} = C_{F,m}$. Therefore, Equation (14) yields

$$J_w = A \left(\pi_{D,b} \frac{1 - \frac{C_{F,b}}{C_{D,b}} \exp(J_w K)}{1 + \frac{B}{J_w} [\exp(J_w K) - 1]} - \Delta P \right) \quad (15)$$

2.2.3. Solution Diffusion Model Development

In the model proposed by Lee et al. [37], the effect of the ECP was neglected. Therefore, later studies proposed several modifications to include the ECP effect in the model.

Achilli's Model

The first modification to the solution diffusion model was proposed by Achilli et al. [38], where the effect of the ECP was considered. The dilutive ECP (at the draw side) was ob-

tained based on film theory, where the osmotic pressure ratio in the draw side boundary layer is given by Equation (16) [39,40]:

$$\frac{\pi_{D,m}}{\pi_{D,b}} = \exp\left(-\frac{J_w}{k_D}\right) \tag{16}$$

where k_D is the mass transfer coefficient of the draw side.

Substituting Equation (16) into Equation (14) (which already considers the ICP effect) and assuming the ratio of the osmotic pressures to be equal to the ratio of the salt concentrations, i.e., $\frac{C_{F,b}}{C_{D,m}} = \frac{\pi_{F,b}}{\pi_{D,m}}$, gives the following equation for the water flux:

$$J_w = A \left(\frac{\pi_{D,b} \exp\left(-\frac{J_w}{k_D}\right) - \pi_{F,b} \exp(J_w K)}{1 + \frac{B}{J_w} [\exp(J_w K) - 1]} - \Delta P \right) \tag{17}$$

Yip’s Model

Another model by Yip et al. [41] considered the effect of the reverse salt flux and ECP by assuming the osmotic pressure to be linearly proportional to the salt concentration. Similar to the ICP effect, the salt flux across the boundary layer (on the draw side) is caused by diffusion and convection, as given by Equation (18):

$$J_s = D \frac{dC(x)}{dx} - J_w C(x) \tag{18}$$

Rearrangement of Equation (18) gives

$$\left(\frac{1}{C + \frac{J_s}{J_w}} \right) dC = \frac{J_w}{D} dx \tag{19}$$

Integrating Equation (19) using the boundary conditions $C(x) = C_{D,m}$ at $x = 0$ and $C(x) = C_{D,b}$ at $x = \delta_D$, where x is the distance measured from the membrane active layer and δ_D is the draw boundary layer thickness, gives the following expression for the draw salt concentration at the membrane surface:

$$C_{D,m} = C_{D,b} \exp\left(J_w \frac{\delta_D}{D}\right) + \frac{J_s}{J_w} \left[\exp\left(J_w \frac{\delta_D}{D}\right) - 1 \right] \tag{20}$$

In Equation (20), the first term on the RHS represents the draw concentration at the membrane surface, while the second term represents the reduction in salt concentration due to the salt flux across the membrane active layer. Subtracting Equation (9) from Equation (20) and substituting J_s from Equation (6) and rearranging yields the following expression:

$$C_{D,m} - C_{icp} = \frac{C_{D,b} \exp\left(-\frac{J_w}{k_D}\right) - C_{F,b} \exp(J_w K)}{1 + \frac{B}{J_w} \left[\exp(J_w K) - \exp\left(-\frac{J_w}{k_D}\right) \right]} \tag{21}$$

where k_D is the mass transfer coefficient of the draw solution ($k_D = D/\delta_D$). Assuming the osmotic pressure difference to be linearly proportional to the salt concentration difference, i.e., $\Delta\pi_m = \Delta C_m$ and substituting Equation (21) into Equation (1) yields the following expression for the water flux:

$$J_w = A \left(\frac{\pi_{D,b} \exp\left(-\frac{J_w}{k_D}\right) - \pi_{F,b} \exp(J_w K)}{1 + \frac{B}{J_w} \left[\exp(J_w K) - \exp\left(-\frac{J_w}{k_D}\right) \right]} - \Delta P \right) \tag{22}$$

Touati’s Model

The previously discussed modifications only considered the effect of the ECP on the draw side, neglecting its effect on the feed side. Touati et al. [42] derived a new expression to account for the effect of the external concentration polarization on both the draw and feed sides, as well as the ICP. Similar to the salt flux calculation on the draw side carried out by Yip et al. [41], the salt flux across the boundary layer on the feed side is given by Equation (18). By integrating Equation (18) using the boundary conditions $C(x) = C_{F,m}$ at $x = 0$ and $C(x) = C_{F,b}$ at $x = \delta_F$, Equation (23) is obtained, where x is the distance from the membrane support layer and δ_F is the feed boundary layer thickness:

$$C_{F,m} = C_{F,b} \exp\left(J_w \frac{\delta_F}{D}\right) + \frac{J_s}{J_w} \left[\exp\left(J_w \frac{\delta_F}{D}\right) - 1 \right] \tag{23}$$

Substituting Equations (9), (20), and (23) into Equation (5) yields

$$\pi_{icp} = \beta R_u T \left[C_{F,b} \exp\left(\frac{J_w}{k_F}\right) + \frac{J_s}{J_w} \left[\exp\left(\frac{J_w}{k_F}\right) - 1 \right] \right] \exp(J_w K) + \frac{J_s}{J_w} [\exp(J_w K) - 1] \tag{24}$$

$$\pi_{D,m} = \beta R_u T C_{D,b} \exp\left(\frac{J_w}{k_D}\right) + \frac{J_s}{J_w} \left[\exp\left(\frac{J_w}{k_D}\right) - 1 \right] \tag{25}$$

The ratio of the salt flux to the water flux is influenced by the water and salt permeability coefficients of the membranes, as shown by Equation (26) [27]. The ratio of the salt flux to the water flux can be solved by combining Equations (4)–(6), yielding the following expression:

$$\frac{J_s}{J_w} = \frac{B}{A \beta R_u T} \left(1 + \frac{A \Delta P}{J_w} \right) \tag{26}$$

By substituting the equations for osmotic pressure (i.e., Equations (24) and (25)) and Equation (26) into Equation (4), the following expression for water flux is obtained:

$$J_w = A \left(\left[\pi_{D,b} + \frac{B}{A} \left(1 + \frac{A \Delta P}{J_w} \right) \right] \exp\left(-\frac{J_w}{k_D}\right) - \left[\pi_{F,b} + \frac{B}{A} \left(1 + \frac{A \Delta P}{J_w} \right) \right] \exp(J_w K) \exp\left(\frac{J_w}{k_F}\right) - \Delta P \right) \tag{27}$$

Comparison between Different Models

A summary of the several modifications to the solution diffusion model is presented in Table 1. Generally, the modified versions of the solution diffusion model predicted results that were closer to those obtained experimentally when the effect of the ECP was considered. The predicted water flux using the different modified versions of the solution diffusion model were compared with the experimental results conducted using a draw solution of 20 g/L NaCl at 20 °C [43]. The comparison is shown in Figure 4. When the effects of both the internal and external concentration polarization were neglected, the water flux was calculated using Equation (1). The average percentage error in the water flux results obtained in this case was around 40%, while the average percentage error for Lee et al. [37] was around 17% when compared with the experimental results. However, for all the modified versions of the solution diffusion model that considered the effect of the ECP, the percentage error obtained was less than 1% when compared with the experimental data. Thus, the modified versions predict water flux values that were very close and displayed a good agreement with experimental data, as shown in Figure 4.

Table 1. Solution diffusion model development.

Model	Model Expression	Assumptions
Lee et al. [37]	$J_w = A \left(\pi_{D,b} \frac{1 - \frac{C_{F,b}}{C_{D,b}} \exp(J_w K)}{1 + \frac{B}{J_w} [\exp(J_w K) - 1]} - \Delta P \right)$	$C_{F,b} = C_{F,m}$ $C_{D,b} = C_{D,m}$
Achilli et al. [38]	$J_w = A \left(\frac{\pi_{D,b} \exp(-\frac{J_w}{k}) - \pi_{F,b} \exp(J_w K)}{1 + \frac{B}{J_w} [\exp(J_w K) - 1]} - \Delta P \right)$	$C_{F,b} = C_{F,m}$ $C_{D,b} \neq C_{D,m}$ $\frac{C_{F,b}}{C_{D,b}} = \frac{\pi_{F,b}}{\pi_{D,b}}$
Yip et al. [41]	$J_w = A \left(\frac{\pi_{D,b} \exp(-\frac{J_w}{k}) - \pi_{F,b} \exp(J_w K)}{1 + \frac{B}{J_w} [\exp(J_w K) - \exp(-\frac{J_w}{k})]} - \Delta P \right)$	$C_{F,b} = C_{F,m}$ $C_{D,b} \neq C_{D,m}$ $\Delta \pi_m = \Delta C_m$
Touati et al. [42]	$J_w = A \left(\left[\pi_{D,b} + \frac{B}{A} \left(1 + \frac{A \Delta P}{J_w} \right) \right] \exp\left(-\frac{J_w}{k_D}\right) - \left[\pi_{F,b} + \frac{B}{A} \left(1 + \frac{A \Delta P}{J_w} \right) \right] \exp(J_w K) \exp\left(\frac{J_w}{k_F}\right) - \Delta P \right)$	$C_{F,b} \neq C_{F,m}$ $C_{D,b} \neq C_{D,m}$ $\pi = \beta R T C$ $k_D \neq k_F$

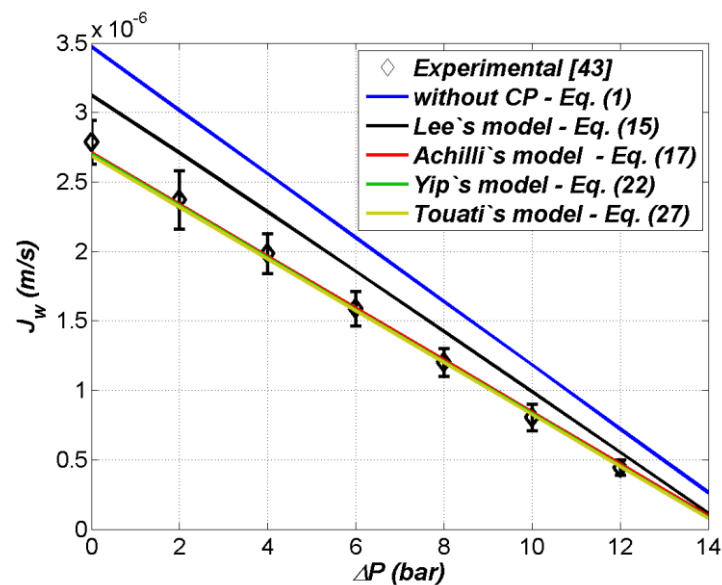


Figure 4. Comparison between the water flux generated using different modifications of the solution diffusion model.

3. PRO Membranes and Modules

The PRO process uses semi-permeable membranes that allow for water flow and prevent salt flow. Membranes suitable for use in PRO should meet several criteria including their ability to withstand relatively high pressure, which optimally should be half of the osmotic pressure [44,45]. The membranes should also have low salt permeability and high water permeability to enhance the water flux [44]. In addition, they should have a low structure parameter to minimize the internal concentration polarization. In most PRO systems, two types of membranes are commonly used, namely, (1) membranes synthesized using cellulose acetate (CA) or cellulose triacetate (CTA) and (2) thin-film composite (TFC) membranes, which include an active nonporous layer on a porous support layer [46,47]. These membranes are arranged in different module designs to maximize the area-to-volume ratio, such as plate-and-frame, hollow fiber, tubular, and spiral wound modules [48,49], as shown in Figure 5. The following section discusses two of these modules, namely, plate-and-frame and spiral wound modules, as plate-and-frame modules are most commonly used in laboratory investigations of PRO, while spiral wound modules were used in pilot PRO power plants.

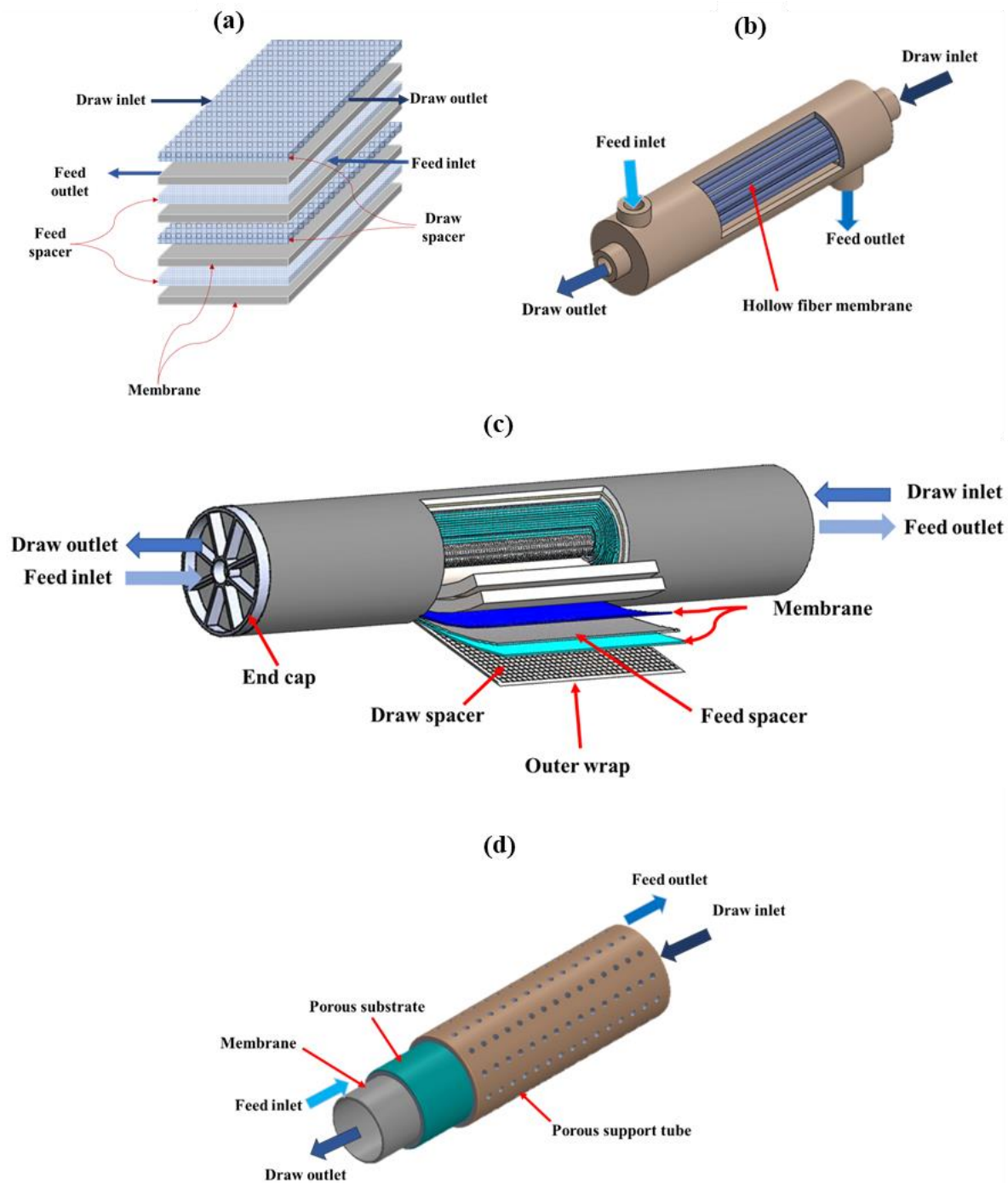


Figure 5. A 3D schematic of the (a) plate-and-frame module, (b) hollow fiber module, (c) spiral wound module, and (d) tubular module.

3.1. Plate-and-Frame Module

A plate-and-frame module (Figure 5a) is the simplest design for packing flat sheet membranes to increase the surface-area-to-volume ratio. In a plate-and-frame module, a membrane is sandwiched between a feed spacer and a draw spacer, and all of these are layered between two end plates. Feed and draw solutions are forced to flow parallel to the membrane surface in their corresponding channels, as shown in Figure 5a. Despite its simple design and easy manufacturing, plate-and-frame modules are not preferable for use in large-scale PRO power plants, as they have a lower surface-area-to-volume ratio

compared with spiral wound and hollow fiber modules [29,30]. The surface-area-to-volume ratio for a plate-and-frame module ranges from 100 to 400 m²/m³ [50].

A single flat sheet membrane module (or membrane cell) is typically used in lab-scale studies to assess the PRO performance and measure membrane properties. Table 2 summarizes the performance and properties of several commercial membranes tested (experimental investigation) and simulated (numerical investigation) in flat sheet membrane modules. The water and salt permeability coefficients (*A* and *B*) and the membrane structure parameter (*S*) were determined by carrying out RO and FO tests using bench-top flat sheet modules. The experimentally determined membrane properties were used in numerical investigations to assess the PRO performance under different operating conditions using the solution diffusion model. The results obtained by the numerical and experimental investigations of flat sheet modules were commonly found to be in good agreement, as the measured and estimated power density are in the same range, as shown in Figure 6. This figure shows that the power densities from a few investigations of a membrane cell that used hypersaline draw solutions were higher than 56.4 W/m², which is considered the minimum power density for PRO to be as cost-effective as solar photovoltaic (PV) panels [51,52].

Table 2. Performance and key properties for commercially available membranes in a single flat sheet membrane module from both experimental and numerical investigations.

Membrane Material	Membrane Area (m ²) × 10 ⁻⁴	Membrane Properties			Operating Conditions		Power Density (W/m ²)	Ref.	
		<i>A</i> (L/m ² hr bar)	<i>B</i> (L/m ² hr)	<i>S</i> (μm)	Concentration (Feed/Draw)	Hydraulic Pressure Difference (bar)			
Experimental investigations	CTA	18.8	0.67	0.40	682	DI/0.6 M NaCl	9.7	2.7	[38]
	CTA	18.8	0.67	0.40	682	DI/1.026 M NaCl	9.7	5.1	[38]
	CTA	140.0	0.37	0.28	590	0.01 M/1 M NaCl	15.0	3.9	[28]
	CTA	140.0	0.44	0.07	1380	0.01 M/1 M NaCl	14.0	3.0	[28]
	CTA	140.0	0.75	0.01	480	0.01 M/1 M NaCl	12.0	4.5	[28]
	CTA	20.0	1.23	2.62	409	0.5 M/1 M NaCl	12.5	0.9	[25]
	CTA	20.0	1.23	2.62	504	0.5 M/1.5 M NaCl	12.5	2.8	[25]
	CTA	20.0	1.23	2.62	505	0.5 M/2 M NaCl	12.5	4.7	[25]
	TFC	20.0	2.49	0.39	564	DI/0.6 M NaCl	13.8	7.5	[53]
	TFC	20.0	2.49	0.39	564	DI/1 M NaCl	20.7	14.1	[53]
	TFC	20.0	2.49	0.39	564	DI/2 M NaCl	41.4	39.4	[53]
	TFC	20.0	2.49	0.39	564	DI/3 M NaCl	48.3	59.7	[53]
	TFC	139.0	1.50	3.74	159	DI/1 M NaCl	10.5	7.0	[54]
	TFC	139.0	1.94	1.99	274	DI/1 M NaCl	10.5	6.8	[54]
	TFC	139.0	1.63	1.42	295	DI/1 M NaCl	21.0	8.3	[54]
	TFC	139.0	1.63	1.42	295	DI/2 M NaCl	35.0	11.5	[54]
	TFC	139.0	1.63	1.42	295	DI/3 M NaCl	41.0	15.5	[54]
	CTA	139.0	0.51	2.19	600	DI/1 M NaCl	19.0	3.8	[54]
	TFC	120.0	2.78	1.36	513	DI/1.2 M NaCl	21.0	15.3	[55]
	TFC	120.0	2.29	0.30	198	DI/1.2 M NaCl	21.0	12.5	[55]
	CTA	120.0	0.77	0.29	408	DI/1.2 M NaCl	21.0	9.8	[55]
	CTA	120.0	0.77	0.29	408	DI/1.2 M NaCl	12.0	6.9	[55]
	TFC	120.0	3.35	1.18	398	DI/1.2 M NaCl	12.0	7.9	[55]
	CTA	33.7	0.42	0.29	1028	DI/3 M NaCl	40.0	10.5	[56]
	CTA	33.7	0.76	0.44	655	DI/3 M NaCl	40.0	30.0	[56]
	CTA	33.7	0.69	0.34	707	DI/3 M NaCl	60.0	32.0	[56]
	TFC	33.7	1.25	0.19	471	DI/3 M NaCl	35.0	27.0	[56]
	TFC	33.7	-	-	-	DI/3 M NaCl	10.0	5.0	[56]
	TFC	87.5	4.21	1.43	267	DI/0.51 M NaCl	6.0	5.0	[57]
	CTA	10.0	0.13	0.02	800	0.008 M/0.6 M NaCl	13.0	2.3	[42]
CTA	10.0	0.38	0.09	1550	0.008 M/0.6 M NaCl	13.0	3.0	[42]	
CTA	10.0	0.38	0.09	1550	0.008 M/1.026 M NaCl	24.0	5.0	[42]	

Table 2. Cont.

Membrane Material	Membrane Area (m ²) × 10 ⁻⁴	Membrane Properties			Operating Conditions		Power Density (W/m ²)	Ref.	
		A (L/m ² hr bar)	B (L/m ² hr)	S (μm)	Concentration (Feed/Draw)	Hydraulic Pressure Difference (bar)			
CA	0.5	0.72	0.22	2500	DI/0.4 M NaCl	7.5	1.6	[58]	
TFC	0.5	2.56	0.40	670	DI/0.48 M NaCl	10.5	2.7	[58]	
CTA	20.0	1.23	2.62	689	DI/0.5 M NaCl	12.5	1.0	[26]	
CTA	20.0	1.23	2.62	689	DI/1 M NaCl	12.5	3.8	[26]	
CTA	20.0	1.23	2.62	689	DI/2 M NaCl	12.5	7.9	[26]	
CTA	140.0	0.8	0.41	652	Tap water/0.17 M NaCl	3.6	0.3	[43]	
CTA	140.0	0.8	0.41	652	Tap water/0.34 M NaCl	7.1	1.2	[43]	
CTA	140.0	0.8	0.41	652	Tap water/0.51 M NaCl	10.7	2.6	[43]	
Numerical investigations	TFC	139.0	1.63	1.42	295	DI/1 M NaCl	24.0	9.0	[54]
	TFC	139.0	1.63	1.42	295	DI/2 M NaCl	52.5	26.0	[54]
	TFC	139.0	1.63	1.42	295	DI/3 M NaCl	87.0	44.0	[54]
	CTA	10.0	0.13	0.02	800	0.008 M/0.6 M NaCl	13.0	2.5	[42]
	CTA	10.0	0.38	0.09	1550	0.008 M/0.6 M NaCl	13.0	3.5	[42]
	CTA	10.0	0.38	0.09	1550	0.008 M/1.026 M NaCl	24.0	5.5	[42]
	CTA	18.8	0.67	0.40	682	DI/0.6 M NaCl	13.0	2.9	[38]
	CTA	18.8	0.67	0.40	646	DI/1.026 M NaCl	23.0	8.0	[38]
	CTA	20.0	1.23	2.62	409	0.5 M/1 M NaCl	10.0	1.0	[25]
	CTA	20.0	1.23	2.62	504	0.5 M/1.5 M NaCl	22.0	3.2	[25]
	CTA	20.0	1.23	2.62	505	0.5 M/2 M NaCl	34.0	6.8	[25]
	TFC	20.0	2.49	0.39	564	DI/0.6 M NaCl	13.8	6.9	[53]
	TFC	20.0	2.49	0.39	564	DI/1 M NaCl	24.0	15.0	[53]
	TFC	20.0	2.49	0.39	564	DI/2 M NaCl	55.0	41.0	[53]
	TFC	20.0	2.49	0.39	564	DI/3 M NaCl	95.0	75.0	[53]
	TFC	20.0	2.49	0.39	564	DI/1 M NaCl	23.0	14.2	[59]
	TFC	20.0	2.49	0.39	564	DI/3 M NaCl	51.0	39.5	[59]
	TFC	20.0	1.23	2.62	689	DI/1 M NaCl	18.2	4.8	[59]
	TFC	20.0	1.23	2.62	689	DI/0.5 M NaCl	8.0	1.6	[59]
	CTA	10.0	0.38	0.09	1550	0.008 M/0.6 M NaCl	12.0	2.5	[60]
CTA	10.0	0.38	0.09	1550	0.008 M/1.2 M NaCl	30.0	12.0	[60]	

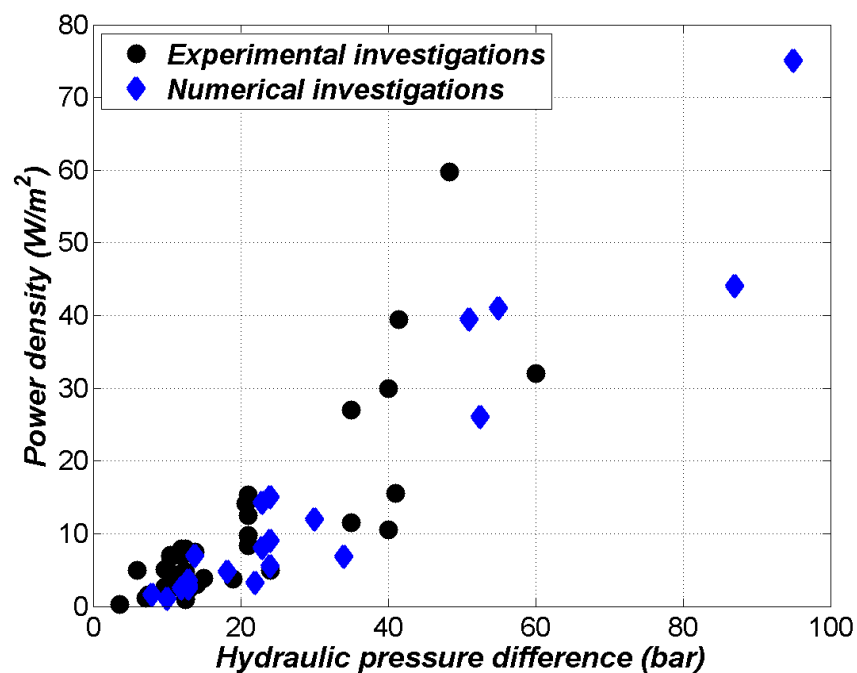


Figure 6. PRO performance from experimental and numerical investigations of a single flat sheet membrane module [25,26,28,38,42,43,53–60]. The data used in this figure are summarized in Table 2.

3.2. Spiral Wound Module (SWM)

The other common module used in PRO systems is the spiral wound module (SWM), which is more suitable for use in large-scale plants since it has a large membrane-area-to-volume ratio ($300\text{--}1000\text{ m}^2/\text{m}^3$) [50]. An SWM consists of several membrane envelopes and spacers wrapped around a perforated tube, as shown in Figure 5c. The commercially available reverse osmosis SWM was modified by Foreman and Worsley [61] to be suitable initially for FO and later for the PRO process. In their design, a central glue line was added to the membrane facing the feed side, causing feed water to flow back to the central tube through a 180-degree turn, as shown in Figure 7. This causes a significant increase in the pressure drop on the feed water side due to the long flow path. In addition, this design was reported to be inadequate for PRO due to the presence of areas of low flow velocity and poor flow distribution [30].

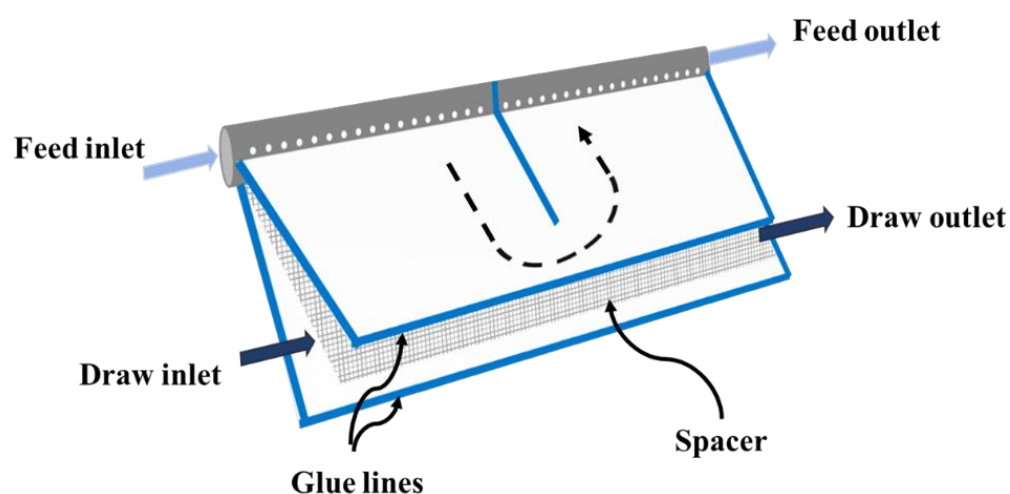


Figure 7. An illustration of the flow path for the commercial SWM.

Several studies experimentally investigated the performance of an SWM working under PRO conditions [29,62–65]. They reported many performance issues, such as the draw solution's high-pressure effect, the deviation between experimental measurements and the model prediction, and differing performance between large and small module areas. Kim et al. [29] experimentally investigated the performance of a PRO-SWM with a membrane area of 29 m^2 . They reported a large increase in the feed solution pressure drop as water flowed through the draw channel. Xu et al. [65] reported a similar increase in the feed solution pressure drop, which was caused by the draw solution's high pressure, when using a PRO-SWM with a membrane area of 0.94 m^2 . The PRO performance of a small SWM module with a membrane area of 0.5 m^2 was investigated both numerically and experimentally by Attarde et al. [62]. Using numerical analysis, they achieved a maximum power density of $3.5\text{ W}/\text{m}^2$; however, they were unable to obtain this power density experimentally due to the hydraulic pressure limit of the membrane (5 bars).

Several studies numerically investigated the performance of an SWM [62,66–69]. The reported power density values of these studies were noticed to be higher compared with the experimental results. Matta et al. [66] numerically investigated the performance of an SWM with a membrane area of 30 m^2 , assuming a linear pressure drop across the length of the membrane. Although the results of their numerical analysis were validated against experimental data of a flat sheet module with an area of 20 cm^2 , their obtained power density was overestimated compared with the experimental results obtained by Kim et al. [29] for the same SWM. Another study by Altaee and Cippolina [67] also overestimated the power density values of a large-scale SWM, which might have been due to the fact that they ignored the effect of the pressure drop along the module, yielding a higher water flux. The overestimation of power density values reported by these numerical

investigations was also reported by Binger and Achilli [68]. They compared the power density obtained by their numerical model to the experimental results of Achilli et al. [63] for a PRO-SWM with an area of 4.18 m². The overestimation of the power density by some numerical investigations of SWM compared with experimental data is clearly shown in Table 3 and Figure 8, where the numerically calculated power density values are higher than the experimentally measured power density for the same membrane properties. Although several numerical SWM investigations predicted a high power density of up to 16 W/m², the highest power density achieved through experimental investigations of the SWM was 3.5 W/m². From Table 3, the results obtained via numerical and experimental investigations of small-scale modules were comparable. However, in large-scale modules, the power density obtained using experimental investigations was considerably lower than those obtained using numerical investigations. This could have been due to the performance of large-scale modules being significantly influenced by the effect of the draw solution's high hydraulic pressure on the feed side pressure drop [29,65]. However, this effect is not significant in the case of small SWM and flat sheet modules. Thus, the effect of the draw hydraulic pressure on feed side pressure drop should be considered in numerical investigations when assessing the performance of a large SWM.

Table 3. Performance and key properties for commercially available membranes in a spiral wound module from both experimental and numerical investigations.

	Membrane Material	Membrane Area (m ²)	Membrane Properties			Operating Conditions		Power Density (W/m ²)	Ref.
			A (L/m ² hr bar)	B (L/m ² hr)	S (μm)	Concentration (Feed/Draw)	Hydraulic Pressure Difference (bar)		
Experimental investigations	TFC	29.0	0.72	0.28	645	0.001 M/0.6 M NaCl	7.7	0.96	[29]
	TFC	29.0	0.72	0.28	645	0.001 M/1.2 M NaCl	15.6	2.10	[29]
	TFC	29.0	0.72	0.28	645	0.001 M/0.52 M NaCl	9.8	0.82	[29]
	TFC	29.0	0.72	0.28	645	0.002 M/0.6 M NaCl	9.8	1.00	[29]
	TFC	29.0	0.72	0.28	645	0.01 M/0.6 M NaCl	9.8	0.91	[29]
	TFC	29.0	0.72	0.28	645	0.05 M/0.6 M NaCl	9.8	0.49	[29]
	TFC	29.0	0.72	0.28	645	0.08 M/0.6 M NaCl	9.8	0.08	[29]
	CTA	0.5	0.63	0.42	496	0.008 M/0.07 M NaCl	1.0	0.02	[62]
	CTA	0.5	0.63	0.42	496	0.008 M/0.1 M NaCl	2.3	0.07	[62]
	CTA	0.5	0.63	0.42	496	0.008 M/0.15 M NaCl	3.4	0.15	[62]
	CTA	0.5	0.63	0.42	496	0.008 M/0.51 M NaCl	4.0	0.56	[62]
	CTA	0.5	0.63	0.42	496	0.008 M/1.026 M NaCl	4.0	1.10	[62]
	CTA	0.9	-	-	-	DI/0.5 M NaCl	4.5	0.40	[65]
	TFC	15.3	-	-	-	Tap water/0.6 M NaCl	12.0	1.40	[64]
	TFC	15.3	-	-	-	Tap water/0.8 M NaCl	12.0	1.64	[64]
	TFC	15.3	-	-	-	Tap water/1.2 M NaCl	16.0	2.33	[64]
	TFC	4.2	5.10	0.09	310	DI/0.48 M NaCl	4.5	1.12 *	[63]
TFC	4.2	5.10	0.09	310	DI/0.48 M NaCl	9.5	3.51 *	[63]	
Numerical investigations	CTA	0.5	0.63	0.42	496	0.008 M/0.07 M NaCl	1.5	0.03	[62]
	CTA	0.5	0.63	0.42	496	0.008 M/0.1 M NaCl	2.3	0.07	[62]
	CTA	0.5	0.63	0.42	496	0.008 M/0.15 M NaCl	3.4	0.15	[62]
	CTA	0.5	0.63	0.42	496	0.008 M/0.51 M NaCl	10.2	0.95	[62]
	CTA	0.5	0.63	0.42	496	0.008 M/1.026 M NaCl	21.0	3.25	[62]
	TFC	4.2	5.10	0.09	310	DI/0.48 M NaCl	8.0	5.10	[68]
	TFC	4.2	5.10	0.09	310	DI/0.48 M NaCl	10.5	9.50	[68]
	TFC	4.2	5.10	0.09	310	DI/0.48 M NaCl	9.5	9.00	[68]
	TFC	4.2	5.10	0.09	310	DI/0.48 M NaCl	11.0	11.00	[68]
	TFC	4.2	5.10	0.09	310	DI/0.48 M NaCl	10.0	10.80	[68]
	CTA	30.0	0.40	0.30	702	0.6 M/2.74 M NaCl	50.0	9.90	[66]
	CTA	30.0	0.40	0.30	702	DI/0.5 M NaCl	9.0	1.75	[66]
	CTA	8.4	3.42	0.31	350	DI/0.6 M NaCl	13.0	16.00	[69]
	N/A	24.0	1.23	2.60	167	0.02 M/1.2 M NaCl	27.5	12.10	[67]
N/A	24.0	1.23	2.60	167	0.02 M/0.6 M NaCl	13.8	3.70	[67]	

* The power density was calculated using the data given in the cited reference to account for the pressure drop.

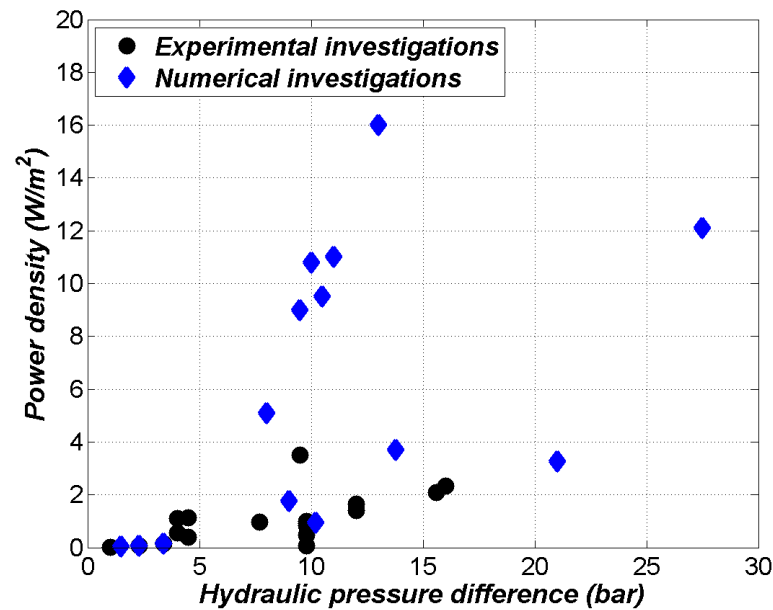


Figure 8. PRO performance from experimental and numerical investigations of a spiral wound module [29,62–69]. The data used in this figure are summarized in Table 3.

4. First PRO Pilot Plant

The first attempt at commercial power generation using PRO was a pilot plant in Norway; it was built by Statkraft in 2009 and later terminated in 2014 [70,71]. They used spiral wound modules with different membrane types and generated power with a power density of 0.9 W/m^2 , which was significantly lower than the expected power density. The inadequate production of energy could have been due to the use of inefficient spacers, as the commercially available spacers are not suitable for PRO application [30]. These spacers lead to severe membrane deformation as the hydraulic draw pressure increases, which blocks the feed channel, increasing the pressure drop on the feed side and reducing the performance [26–28,53]. Moreover, the module design used was reported to be unsuitable, as it resulted in the presence of areas of low flow velocity and poor flow distribution [30]. Another important factor that influenced the power density generated was the effect of the draw solution dilution [17,59]. Throughout the length of the membrane, the effective osmotic pressure difference decreases from the inlet to the outlet. This effect is more pronounced in PRO systems with a large membrane area due to the large changes in salt concentrations at both the draw and feed sides. Additionally, the presence of both internal and external concentration polarization, as well as membrane fouling, which could be reduced but not eliminated by regular cleaning, reduces the performance of PRO systems [32,33,72]. The inefficiency of the first PRO power plant prototype indicated the need to optimize the design of PRO membranes, modules, spacers, and operating conditions to reach the power-generating potential of PRO. This encouraged several efforts to enhance the design of modules and spacers to enhance PRO performance [73,74]. Some of these efforts included studies that improved the design of SWMs by modifying the central tubes [75] and modifying the arrangement of the membrane and spacers [76–78]. New module designs were also proposed, such as those consisting of a stack of membrane plate assemblies [79]. Moreover, to reduce membrane damage and increase its mechanical strength, a woven or non-woven mesh was added as membrane support [80], or a base layer with mechanical reinforcement was added [81]. However, despite these notable efforts, PRO commercialization is yet to be achieved.

5. PRO Challenges

5.1. Concentration Polarization

Concentration polarization is the accumulation or depletion of solutes near the membrane interface due to water flow from the feed side to the draw side of the membrane. Thus, creating a smaller concentration difference across the membrane active layer when compared with the bulk concentration difference across the membrane, which negatively affects the overall performance [82,83]. Concentration polarization can either be internal, which occurs inside the membrane support layer, or external, which occurs near the membrane surface, as shown in Figure 3. The presence of internal concentration polarization in the support layer occurs due to the accumulation of salts in the active–support layer interface, and this concentration is represented by C_{icp} . This reduces the effective osmotic pressure difference across the active membrane layer and consequently reduces the water flux across the membrane. The internal concentration polarization is controlled by the membrane structure parameter (S), which is the characteristic length that an ion diffuses through in the membrane support layer to reach the feed solution side [43,84]. With a lower structure parameter, the internal concentration polarization is reduced. On the other hand, external concentration polarization can be either concentrative or dilutive. As water flows from the feed to the draw side, an increase in the concentration at the support layer surface occurs ($C_{F,b}$ to $C_{F,m}$), i.e., concentrative external concentration polarization, and a decrease in the concentration at the active layer surface occurs ($C_{D,b}$ to $C_{D,m}$), i.e., dilutive external concentration polarization. External concentration polarization can be controlled by introducing turbulence near the membrane surface through membrane spacers. The combined effect of both the internal and external concentration polarization results in the reduction of the effective driving force from the difference in bulk concentrations ($C_{D,b}-C_{F,b}$) to the difference in concentrations across the membrane active layer ($C_{D,m}-C_{icp}$).

5.2. Pressure Drop

Membrane spacers play an important role in modules, as they introduce turbulence at the membrane surface, which decreases the external concentration polarization [85–87]. However, these spacers can have a negative effect on the performance, as they cause a significant increase in the pressure drop [88–90]. The pressure drop has a significant effect on the water flux, as it affects the hydraulic pressure difference across the membrane [91–97]. Therefore, the effect of the pressure drop along the flow channels should be considered in water flux calculations when modeling the PRO process. The pressure drop along the flow channels was measured experimentally for several spacer geometries at different velocities [86,98,99]. The measurements were conducted using a rectangular channel filled with a spacer or using an RO membrane module. Therefore, the effect of the spacer elastic deformation due to high pressure and a membrane indentation depth was not considered in these measurements. The pressure drop measurements were then used to develop empirical correlations for the friction factor as a function of the Reynolds number. The correlations were used by several studies to estimate the pressure drop in actual membrane modules with both small and large membrane areas to assess the PRO performance [100–103]. It is important to emphasize that these empirical correlations can only be used to estimate the pressure drop across a channel with the same spacer used in the experimental measurement and without the effect of elastic deformation of the spacer and membrane indentation depth under high operating pressure. Even though there are numerous correlations for spacers with different characteristics [104,105], a general correlation is needed that can be used with currently available PRO spacers.

An alternative approach for estimating the pressure drop across a channel is using computational fluid dynamics (CFD) in either a simplified 2D model or a detailed 3D model [103,106–110]. The simplified 2D model was utilized by several studies to investigate the concentration, pressure drop, and flow distribution [111–114]. Spacers with a triangular filament cross-section geometry were reported to be more efficient at reducing the concentration polarization when compared with spacers with different geometries [115].

Although 2D models can allow for the quick estimation of the pressure drop for different spacers, a drawback to 2D models is their lack of ability to accurately estimate the pressure drop for spacers with complex geometrical features. On the other hand, 3D models allow for an accurate estimation of the pressure drop, as complex geometrical features, such as the filament intersection, angle of attack, and mesh angle, are taken into consideration [103,109,116–120]. Three-dimensional CFD simulations were conducted by drawing cylindrical filaments in a crossing arrangement or using captured microscopic images of the spacer as the geometry of the computational domain. This latter approach was used by Piciooreanu et al. [118], who reported the pressure drop after considering the variation in filament diameters at the intersections to be twice that of the geometry based on a crossing arrangement of cylindrical filaments. However, it is worth mentioning that 3D simulations can be time-consuming and may require high computational power. Moreover, the geometries of commercially available spacers tend to be more complex than spacers with a crossing arrangement of filaments. This could be explained by the change in diameter at the filament intersection [118,121]. An alternative approach for pressure drop estimation across a channel is by treating spacer-filled channels as porous media and using Darcy–Forchheimer equations and CFD simulations [90]. This approach allows for the incorporation of the complex geometrical features of spacers without the need for high computational power. However, the main drawback to this approach is the necessity to estimate both the permeability and inertia coefficients.

5.3. Draw Pressure Effect on Feed Channel Hydrodynamics

High draw pressure affects feed channel hydrodynamics, as it reduces the feed channel gap, thus increasing the pressure drop significantly, which reduces the PRO performance. Karabelas et al. [122] investigated the effect of the draw pressure on the feed channel gap and reported that it is influenced by the indentation depth and reduction in spacer thickness, as shown in Figure 9. The indentation depth can be defined as the depth of the membrane that is deformed due to the applied pressure. Moreover, the reduction in spacer thickness is a result of the elastic deformation of the spacer due to the applied pressure. These effects caused a reduction of around 16% in the effective feed channel gap as draw pressure increased from 1 to 3 bar. Another approach to study the effect of draw hydraulic pressure on the feed channel hydrodynamics was used by Jeon et al. [123], where they changed the draw pressure and measured the feed pressure drop experimentally. Using these results, they developed a correlation to estimate the feed pressure drop using draw solution pressure. However, the draw pressure used by both studies was lower (by up to 3 bars) when compared with the usual operating draw pressure used in PRO [122,123]. She et al. [27] investigated the effect of the feed spacer geometry on the PRO performance. It was reported that feed spacers with large openings resulted in severe membrane deformation, increasing the pressure drop in the feed channel and reducing the power density significantly. Thus, the effect of the draw solution pressure on the effective feed channel gap, which significantly increases the feed pressure drop, should be considered when optimizing the PRO performance, as it is noticeable in large-scale modules.

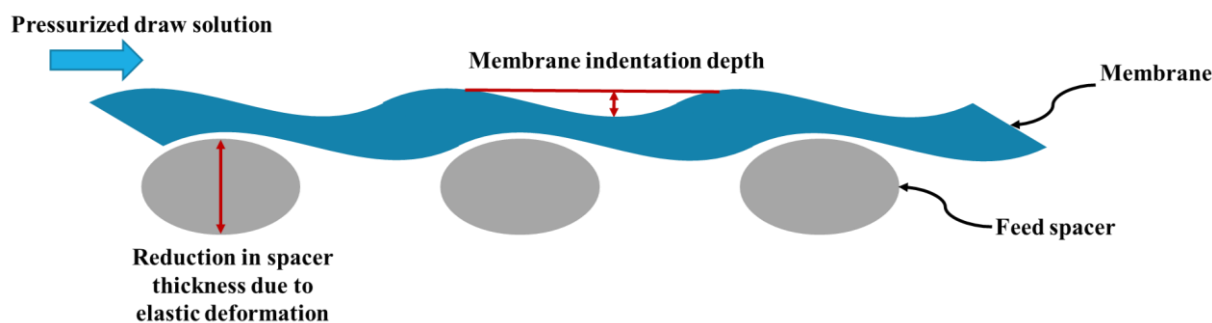


Figure 9. Effect of the draw solution's high pressure on the feed channel hydrodynamics.

5.4. Temperature Variation Effect

The feed and draw solution temperatures can greatly influence the PRO performance. Water temperatures can fluctuate with changes in seasonal temperature and geographical location, affecting the temperature of the water used as the draw or feed in a PRO power plant [124,125]. A solution's temperature can influence its properties, such as the density, diffusion coefficient, viscosity, and osmotic pressure. The solution temperature also affects a membrane's geometrical characteristics, such as its thickness, porosity, and pore size. Moreover, membrane properties, such as water and salt permeabilities, were reported to increase with increasing temperature [125,126]. However, some studies reported a decrease in salt permeability with increasing temperature [127]. The membrane structure parameter, on the other hand, was reported to decrease with increasing temperature by some studies [125], while others reported no change in the structure parameter with temperature [126]. Thus, due to the disagreement in the literature on the effect of temperature on membrane parameters, further studies are required to properly understand the effect of temperature on membrane parameters. Increases in water temperature were shown to enhance the power density in several studies [125,126]. However, the increase in power density with increasing water temperature was reported to be more profound at low draw solution concentrations [25]. Therefore, due to the noticeable effect of temperature on the PRO performance, changes in solution temperatures should be considered when designing PRO systems or when assessing their performance.

6. Conclusions and Recommendations

Despite being recognized as a promising technique to generate power, the commercialization of PRO is currently facing many obstacles. One major challenge is the suboptimal performance of the commercially available membranes when used in PRO systems, as some of these membranes were developed for other applications. Membrane selection in PRO is based on the concentration difference used, which determines the required operating pressure difference. With an increasing concentration difference, the optimal hydraulic pressure difference increases, requiring a membrane that can withstand high pressures. These membranes usually include a thick support layer, which can negatively affect the PRO performance by increasing the effect of the internal concentration polarization. Conversely, at a lower concentration difference, an optimal membrane would possess a thin support layer to reduce the effect of the internal concentration polarization. Therefore, a broad selection of commercially available membranes that are suitable for the wide range of concentration differences can substantially aid PRO commercialization.

Other important challenges to commercialization are the inadequacy of the available feed spacer and module designs for use in PRO systems. Due to the high pressure in the draw channel, feed spacers are compressed, decreasing the effective feed channel height, which significantly increases the pressure drop on the feed side. This phenomenon has not been thoroughly investigated, as it is specific to the PRO process while being absent in RO systems and negligible in FO due to the absence of the large hydraulic pressure difference. Although many 2D CFD simulations were conducted to model the performance of spacers, they could not accurately estimate the pressure drop for spacers with complex geometrical features. On the other hand, 3D models can be time-consuming and require high computational power. Thus, it is necessary to develop appropriate feed spacers that are able to withstand high draw pressures without significantly decreasing the effective feed channel gap. Similarly, the development of a suitable module design is required to facilitate PRO commercialization, as the commercially available spiral wound module is not adequate for PRO systems. This can be explained by the unfavorable flow pattern on the feed side, which results in a high pressure drop and the presence of areas of low velocity.

Although PRO commercialization is a remote prospect, notable advancements in membrane development are present. This can be seen in the abundance of lab-synthesized membranes developed for different concentration differences, which are yet to be commer-

cialized. On the other hand, there is a lack of research efforts aimed at improving spacers and module designs for use in PRO. Therefore, future research should focus on developing appropriate spacers and modules to achieve successful PRO commercialization.

Funding: This research was funded by the Natural Sciences and Engineering Research Council of Canada (NSERC) grant #401366.

Data Availability Statement: The data presented in this study are available in (1) Abdelkader, B.A., 2022, Experimental and Numerical Investigations of Salinity Gradient Energy Harvesting by Pressure Retarded Osmosis, PhD thesis, University of Guelph, Guelph. <https://hdl.handle.net/10214/27156> (accessed on 28 August 2022) and (2) Abdelkader, B.A.; Sharqawy, M.H. Temperature effects on salinity gradient energy harvesting and utilized membrane properties—Experimental and numerical investigation. *Sustain. Energy Technol. Assess.* 2021, 48, 101666. <https://doi.org/10.1016/j.seta.2021.101666>.

Conflicts of Interest: The authors declare no conflict of interest.

Nomenclature

A	Membrane water permeability	$\text{m/s}\cdot\text{Pa}$
B	Membrane salt permeability	m/s
C	Concentration	g/kg
D	Diffusion coefficient	m^2/s
J	Flow flux	m/s
K	Solute resistivity	s/m
k	Mass transfer coefficient	m/s
P	Hydraulic pressure	Pa
R	Universal gas constant	$\text{J/mol}\cdot\text{K}$
S	Structure parameter	m
t	Membrane thickness	m
W	Power density	W/m^2
Greek symbols		
β	van't Hoff coefficient	-
ε	Porosity	-
π	Osmotic pressure	Pa
τ	Tortuosity	-
Subscripts		
b	Bulk	
D	Draw solution	
F	Feed solution	
icp	Active-support layer interface	
m	Membrane surface	
s	Salt or solute	
w	Water	

References

1. Pattle, R.E. Production of Electric Power by mixing Fresh and Salt Water in the Hydroelectric Pile. *Nature* **1954**, *174*, 660. [[CrossRef](#)]
2. Lee, C.; Chae, S.H.; Yang, E.; Kim, S.; Kim, J.H.; Kim, I.S. A comprehensive review of the feasibility of pressure retarded osmosis: Recent technological advances and industrial efforts towards commercialization. *Desalination* **2020**, *491*, 114501. [[CrossRef](#)]
3. Jia, Z.; Wang, B.; Song, S.; Fan, Y. Blue energy: Current technologies for sustainable power generation from water salinity gradient. *Renew. Sustain. Energy Rev.* **2014**, *31*, 91–100. [[CrossRef](#)]
4. Chung, T.-S. *Membrane Technology for Osmotic Power Generation by Pressure Retarded Osmosis*, 1st ed.; CRC Press: New York, NY, USA, 2020. [[CrossRef](#)]
5. Hatzell, M.C.; Cusick, R.D.; Logan, B.E. Capacitive mixing power production from salinity gradient energy enhanced through exoelectrogen-generated ionic currents. *Energy Environ. Sci.* **2014**, *7*, 1159–1165. [[CrossRef](#)]
6. Jones, A.; Finley, W. Recent development in salinity gradient power. In Proceedings of the Oceans 2003: Celebrating the Past—Teaming Toward the Future, San Diego, CA, USA, 22–26 September 2003; Volume 4, pp. 2284–2287. [[CrossRef](#)]
7. Yip, N.Y.; Brogioli, D.; Hamelers, H.V.M.; Nijmeijer, K. Salinity Gradients for Sustainable Energy: Primer, Progress, and Prospects. *Environ. Sci. Technol.* **2016**, *50*, 12072–12094. [[CrossRef](#)] [[PubMed](#)]

8. Sharma, M.; Das, P.P.; Chakraborty, A.; Purkait, M.K. Clean energy from salinity gradients using pressure retarded osmosis and reverse electrodialysis: A review. *Sustain. Energy Technol. Assess.* **2021**, *49*, 101687. [[CrossRef](#)]
9. Yip, N.Y.; Elimelech, M. Comparison of Energy Efficiency and Power Density in Pressure Retarded Osmosis and Reverse Electrodialysis. *Environ. Sci. Technol.* **2014**, *48*, 11002–11012. [[CrossRef](#)]
10. Helfer, F.; Lemckert, C.; Anissimov, Y.G. Osmotic power with Pressure Retarded Osmosis: Theory, performance and trends—A review. *J. Membr. Sci.* **2014**, *453*, 337–358. [[CrossRef](#)]
11. Cath, T.Y.; Childress, A.E.; Elimelech, M. Forward osmosis: Principles, applications, and recent developments. *J. Membr. Sci.* **2006**, *281*, 70–87. [[CrossRef](#)]
12. Sarp, S.; Li, Z.; Saththasivam, J. Pressure Retarded Osmosis (PRO): Past experiences, current developments, and future prospects. *Desalination* **2016**, *389*, 2–14. [[CrossRef](#)]
13. Chung, T.-S.; Luo, L.; Wan, C.F.; Cui, Y.; Amy, G. What is next for forward osmosis (FO) and pressure retarded osmosis (PRO). *Sep. Purif. Technol.* **2015**, *156*, 856–860. [[CrossRef](#)]
14. Bogler, A.; Lin, S.; Bar-Zeev, E. Biofouling of membrane distillation, forward osmosis and pressure retarded osmosis: Principles, impacts and future directions. *J. Membr. Sci.* **2017**, *542*, 378–398. [[CrossRef](#)]
15. Altaee, A.; Sharif, A. Pressure retarded osmosis: Advancement in the process applications for power generation and desalination. *Desalination* **2015**, *356*, 31–46. [[CrossRef](#)]
16. Abdelkader, B.A.; Sharqawy, M.H. Ecological Potential of Osmotic Power Generation by Pressure Retarded Osmosis in Ontario, Canada. In Proceedings of the 4th International Conference on Energy Harvesting, Storage, and Transfer (EHST'20), Ottawa, ON, Canada, 18–19 June 2019. [[CrossRef](#)]
17. Zadeh, A.E.; Touati, K.; Mulligan, C.N.; McCutcheon, J.R.; Rahaman, S. Closed-loop pressure retarded osmosis draw solutions and their regeneration processes: A review. *Renew. Sustain. Energy Rev.* **2022**, *159*, 112191. [[CrossRef](#)]
18. Yip, N.Y.; Elimelech, M. Thermodynamic and Energy Efficiency Analysis of Power Generation from Natural Salinity Gradients by Pressure Retarded Osmosis. *Environ. Sci. Technol.* **2012**, *46*, 5230–5239. [[CrossRef](#)]
19. Loeb, S. Method and Apparatus for Generating Power Utilizing Pressure-Retarded-Osmosis. U.S. Patent US3906250A, 16 September 1975.
20. Loeb, S. Large-scale power production by pressure-retarded osmosis, using river water and sea water passing through spiral modules. *Desalination* **2002**, *143*, 115–122. [[CrossRef](#)]
21. Touati, K.; Tadeo, F.; Chae, S.H.; Kim, J.H.; Alvarez-Silva, O. *Pressure Retarded Osmosis: Renewable Energy Generation and Recovery*, 1st ed.; Academic Press: Cambridge, MA, USA, 2017.
22. Kim, J.; Jeong, K.; Park, M.J.; Shon, H.K.; Kim, J.H. Recent Advances in Osmotic Energy Generation via Pressure-Retarded Osmosis (PRO): A Review. *Energies* **2015**, *8*, 11821–11845. [[CrossRef](#)]
23. Sharqawy, M.H.; Zubair, S.M.; Lienhard, J.H. Energy utilization from disposed brine of desalination plants. In Proceedings of the International Mechanical Engineering Congress & Exposition, Houston, TX, USA, 9–15 November 2012; pp. 1–9.
24. Bajraktari, N.; Hélix-Nielsen, C.; Madsen, H.T. Pressure retarded osmosis from hypersaline sources—A review. *Desalination* **2017**, *413*, 65–85. [[CrossRef](#)]
25. Kim, Y.C.; Elimelech, M. Potential of osmotic power generation by pressure retarded osmosis using seawater as feed solution: Analysis and experiments. *J. Membr. Sci.* **2013**, *429*, 330–337. [[CrossRef](#)]
26. Kim, Y.C.; Elimelech, M. Adverse Impact of Feed Channel Spacers on the Performance of Pressure Retarded Osmosis. *Environ. Sci. Technol.* **2012**, *46*, 4673–4681. [[CrossRef](#)]
27. She, Q.; Hou, D.; Liu, J.; Tan, K.H.; Tang, C.Y. Effect of feed spacer induced membrane deformation on the performance of pressure retarded osmosis (PRO): Implications for PRO process operation. *J. Membr. Sci.* **2013**, *445*, 170–182. [[CrossRef](#)]
28. She, Q.; Jin, X.; Tang, C.Y. Osmotic power production from salinity gradient resource by pressure retarded osmosis: Effects of operating conditions and reverse solute diffusion. *J. Membr. Sci.* **2012**, *401–402*, 262–273. [[CrossRef](#)]
29. Kim, Y.C.; Kim, Y.; Oh, D.; Lee, K.H. Experimental Investigation of a Spiral-Wound Pressure-Retarded Osmosis Membrane Module for Osmotic Power Generation. *Environ. Sci. Technol.* **2013**, *47*, 2966–2973. [[CrossRef](#)] [[PubMed](#)]
30. Nielsen, W.K. Progress in the Development of Osmotic Power. In Proceedings of the Qingdao International Conference on Desalination and Water Reuse, Qingdao, China, 20–23 June 2011.
31. Kim, J.; Lee, J.; Kim, J.H. Overview of pressure-retarded osmosis (PRO) process and hybrid application to sea water reverse osmosis process. *Desalin. Water Treat.* **2012**, *43*, 193–200. [[CrossRef](#)]
32. Fang, L.-F.; Cheng, L.; Jeon, S.; Wang, S.-Y.; Takahashi, T.; Matsuyama, H. Effect of the supporting layer structures on antifouling properties of forward osmosis membranes in AL-DS mode. *J. Membr. Sci.* **2018**, *552*, 265–273. [[CrossRef](#)]
33. Yang, T.; Wan, C.F.; Xiong, J.Y.; Chung, T.-S. Pre-treatment of wastewater retentate to mitigate fouling on the pressure retarded osmosis (PRO) process. *Sep. Purif. Technol.* **2019**, *215*, 390–397. [[CrossRef](#)]
34. Shi, Y.; Zhang, M.; Zhang, H.; Yang, F.; Tang, C.Y.; Dong, Y. Recent development of pressure retarded osmosis membranes for water and energy sustainability: A critical review. *Water Res.* **2020**, *189*, 116666. [[CrossRef](#)]
35. Einarsson, S.J.; Wu, B. Thermal associated pressure-retarded osmosis processes for energy production: A review. *Sci. Total Environ.* **2020**, *757*, 143731. [[CrossRef](#)]
36. NASA Earth Observatory. Sea Surface Temperatures. 2021. Available online: <https://earthobservatory.nasa.gov/global-maps/MYD28M> (accessed on 16 September 2022).

37. Lee, K.; Baker, R.; Lonsdale, H. Membranes for power generation by pressure-retarded osmosis. *J. Membr. Sci.* **1981**, *8*, 141–171. [[CrossRef](#)]
38. Achilli, A.; Cath, T.Y.; Childress, A.E. Power generation with pressure retarded osmosis: An experimental and theoretical investigation. *J. Membr. Sci.* **2009**, *343*, 42–52. [[CrossRef](#)]
39. Elimelech, M.; Bhattacharjee, S. A novel approach for modeling concentration polarization in crossflow membrane filtration based on the equivalence of osmotic pressure model and filtration theory. *J. Membr. Sci.* **1998**, *145*, 223–241. [[CrossRef](#)]
40. Gekas, V.; Hallström, B. Mass transfer in the membrane concentration polarization layer under turbulent cross flow: I. Critical literature review and adaptation of existing Sherwood correlations to membrane operations. *J. Membr. Sci.* **1987**, *30*, 153–170. [[CrossRef](#)]
41. Yip, N.Y.; Elimelech, M. Performance Limiting Effects in Power Generation from Salinity Gradients by Pressure Retarded Osmosis. *Environ. Sci. Technol.* **2011**, *45*, 10273–10282. [[CrossRef](#)] [[PubMed](#)]
42. Touati, K.; Hänel, C.; Tadeo, F.; Schiestel, T. Effect of the feed and draw solution temperatures on PRO performance: Theoretical and experimental study. *Desalination* **2015**, *365*, 182–195. [[CrossRef](#)]
43. Abdelkader, B.A.; Sharqawy, M.H. Temperature effects on salinity gradient energy harvesting and utilized membrane properties—Experimental and numerical investigation. *Sustain. Energy Technol. Assess.* **2021**, *48*, 101666. [[CrossRef](#)]
44. Zhang, S.; Chung, T.-S. Minimizing the Instant and Accumulative Effects of Salt Permeability to Sustain Ultrahigh Osmotic Power Density. *Environ. Sci. Technol.* **2013**, *47*, 10085–10092. [[CrossRef](#)]
45. Han, G.; Wang, P.; Chung, T.-S. Highly Robust Thin-Film Composite Pressure Retarded Osmosis (PRO) Hollow Fiber Membranes with High Power Densities for Renewable Salinity-Gradient Energy Generation. *Environ. Sci. Technol.* **2013**, *47*, 8070–8077. [[CrossRef](#)]
46. Sun, S.-P.; Chung, T.-S. Outer-Selective Pressure-Retarded Osmosis Hollow Fiber Membranes from Vacuum-Assisted Interfacial Polymerization for Osmotic Power Generation. *Environ. Sci. Technol.* **2013**, *47*, 13167–13174. [[CrossRef](#)]
47. Gonzales, R.R.; Park, M.J.; Bae, T.-H.; Yang, Y.; Abdel-Wahab, A.; Phuntsho, S.; Shon, H.K. Melamine-based covalent organic framework-incorporated thin film nanocomposite membrane for enhanced osmotic power generation. *Desalination* **2019**, *459*, 10–19. [[CrossRef](#)]
48. Cui, Z.; Jiang, Y.; Field, R. Fundamentals of Pressure-Driven Membrane Separation Processes. *Membr. Technol.* **2010**, 1–18. [[CrossRef](#)]
49. Naguib, M.F.; Maisonneuve, J.; Laflamme, C.B.; Pillay, P. Modeling pressure-retarded osmotic power in commercial length membranes. *Renew. Energy* **2015**, *76*, 619–627. [[CrossRef](#)]
50. Lee, S. Performance Comparison of Spiral-Wound and Plate-and-Frame Forward Osmosis Membrane Module. *Membranes* **2020**, *10*, 318. [[CrossRef](#)] [[PubMed](#)]
51. Chung, H.W.; Swaminathan, J.; Banchik, L.D.; Lienhard, J.H. Economic framework for net power density and levelized cost of electricity in pressure-retarded osmosis. *Desalination* **2018**, *448*, 13–20. [[CrossRef](#)]
52. Chung, H.W.; Banchik, L.D.; Swaminathan, J. On the present and future economic viability of stand-alone pressure-retarded osmosis. *Desalination* **2017**, *408*, 133–144. [[CrossRef](#)]
53. Straub, A.P.; Yip, N.Y.; Elimelech, M. Raising the Bar: Increased Hydraulic Pressure Allows Unprecedented High Power Densities in Pressure-Retarded Osmosis. *Environ. Sci. Technol. Lett.* **2013**, *1*, 55–59. [[CrossRef](#)]
54. Hickenbottom, K.L.; Vanneste, J.; Elimelech, M.; Cath, T.Y. Assessing the current state of commercially available membranes and spacers for energy production with pressure retarded osmosis. *Desalination* **2016**, *389*, 108–118. [[CrossRef](#)]
55. Plata, S.L.; Childress, A.E. Limiting power density in pressure-retarded osmosis: Observation and implications. *Desalination* **2019**, *467*, 51–56. [[CrossRef](#)]
56. Madsen, H.T.; Nissen, S.S.; Muff, J.; Søgaard, E.G. Pressure retarded osmosis from hypersaline solutions: Investigating commercial FO membranes at high pressures. *Desalination* **2017**, *420*, 183–190. [[CrossRef](#)]
57. Maisonneuve, J.; Laflamme, C.B.; Pillay, P. Experimental investigation of pressure retarded osmosis for renewable energy conversion: Towards increased net power. *Appl. Energy* **2015**, *164*, 425–435. [[CrossRef](#)]
58. Thorsen, T.; Holt, T. The potential for power production from salinity gradients by pressure retarded osmosis. *J. Membr. Sci.* **2009**, *335*, 103–110. [[CrossRef](#)]
59. Manzoor, H.; Selam, M.A.; Rahman, F.B.A.; Adham, S.; Castier, M.; Abdel-Wahab, A. A tool for assessing the scalability of pressure-retarded osmosis (PRO) membranes. *Renew. Energy* **2019**, *149*, 987–999. [[CrossRef](#)]
60. Abdelkader, B.; Sharqawy, M.H. Temperature Effects and Entropy Generation of Pressure Retarded Osmosis Process. *Entropy* **2019**, *21*, 1158. [[CrossRef](#)]
61. Foreman, G.E.; Worsley, P.K. Spiral Wound Membrane Module for Direct Osmosis Separations. U.S. Patent US4033878A, 5 July 1977.
62. Attarde, D.; Jain, M.; Chaudhary, K.; Gupta, S.K. Osmotically driven membrane processes by using a spiral wound module—Modeling, experimentation and numerical parameter estimation. *Desalination* **2015**, *361*, 81–94. [[CrossRef](#)]
63. Achilli, A.; Prante, J.L.; Hancock, N.T.; Maxwell, E.B.; Childress, A.E. Experimental Results from RO-PRO: A Next Generation System for Low-Energy Desalination. *Environ. Sci. Technol.* **2014**, *48*, 6437–6443. [[CrossRef](#)] [[PubMed](#)]
64. Kakihana, Y.; Jullok, N.; Shibuya, M.; Ikebe, Y.; Higa, M. Comparison of Pressure-Retarded Osmosis Performance between Pilot-Scale Cellulose Triacetate Hollow-Fiber and Polyamide Spiral-Wound Membrane Modules. *Membranes* **2021**, *11*, 177. [[CrossRef](#)]

65. Xu, Y.; Peng, X.; Tang, C.Y.; Fu, Q.S.; Nie, S. Effect of draw solution concentration and operating conditions on forward osmosis and pressure retarded osmosis performance in a spiral wound module. *J. Membr. Sci.* **2010**, *348*, 298–309. [[CrossRef](#)]
66. Matta, S.M.; Selam, M.A.; Manzoor, H.; Adham, S.; Shon, H.K.; Castier, M.; Abdel-Wahab, A. Predicting the performance of spiral-wound membranes in pressure-retarded osmosis processes. *Renew. Energy* **2022**, *189*, 66–77. [[CrossRef](#)]
67. Altaee, A.; Cipolina, A. Modelling and optimization of modular system for power generation from a salinity gradient. *Renew. Energy* **2019**, *141*, 139–147. [[CrossRef](#)]
68. Binger, Z.M.; Achilli, A. Forward osmosis and pressure retarded osmosis process modeling for integration with seawater reverse osmosis desalination. *Desalination* **2020**, *491*, 114583. [[CrossRef](#)]
69. Hong, S.-S.; Ryoo, W.; Chun, M.-S.; Lee, S.O.; Chung, G.-Y. Numerical studies on the pressure-retarded osmosis (PRO) system with the spiral wound module for power generation. *Desalin. Water Treat.* **2013**, *52*, 6333–6341. [[CrossRef](#)]
70. Skilhagen, S.E. Osmotic power—A new, renewable energy source. *Desalin. Water Treat.* **2010**, *15*, 271–278. [[CrossRef](#)]
71. Gerstandt, K.; Peinemann, K.-V.; Skilhagen, S.E.; Thorsen, T.; Holt, T. Membrane processes in energy supply for an osmotic power plant. *Desalination* **2008**, *224*, 64–70. [[CrossRef](#)]
72. Alsvik, I.L.; Hägg, M.-B. Pressure Retarded Osmosis and Forward Osmosis Membranes: Materials and Methods. *Polymers* **2013**, *5*, 303–327. [[CrossRef](#)]
73. Reddy, D.; Moon, T.Y.; Reineke, C.E. Counter Current Dual-Flow Spiral Wound Dual-Pipe Membrane Separation. U.S. Patent US5034126A, 23 July 1991.
74. Mcginnis, R.L. Spiral Wound Membrane Module for Forward Osmotic Use. U.S. Patent US20110036774A1, 17 February 2011.
75. Uda, Y.; Kobuke, M. Spiral-Wound Forward Osmosis Membrane Element and Forward Osmosis Membrane Module. U.S. Patent US9861938B2, 9 January 2018.
76. Herron, J.R. Forward Osmosis and Pressure Retarded Osmosis Spacer. WO2014107464A1, 10 July 2014.
77. Sun, G.; Yang, Z. Spiral Wound Membrane Rolls and Modules. WO2018153978A1, 30 August 2018.
78. Lee, S.Y.; Sim, Y.J.; Lee, J.H. Porous Outflow Pipe for Forward Osmosis or Pressure-Retarded Osmosis, and Forward Osmosis or Pressure-Retarded Osmosis Module Comprising Same. U.S. Patent US 11,020,705 B2, 1 June 2021.
79. Benton, C.; Bakajin, O. Separation Systems, Elements, and Methods for Separation Utilizing Stacked Membranes and Spacers. U.S. Patent US 2020/0094193 A1, 17 August 2020.
80. Revanur, R.; Roh, I.; Klare, J.E.; Noy, A.; Bakajin, O. Thin Film Composite Membranes for Forward Osmosis, and Their Preparation Methods. U.S. Patent US20120080378A1, 5 April 2012.
81. Tang, C.; She, Q.; Ma, N.; Wei, J.; Sim, S.T.V.; Fane, A.G. Reinforced Membranes for Producing Osmotic Power in Pressure Retarded Osmosis. U.S. Patent US20150217238A1, 6 August 2015.
82. Tawalbeh, M.; Al-Othman, A.; Abdelwahab, N.; Alami, A.H.; Olabi, A.G. Recent developments in pressure retarded osmosis for desalination and power generation. *Renew. Sustain. Energy Rev.* **2020**, *138*, 110492. [[CrossRef](#)]
83. AlZainati, N.; Saleem, H.; Altaee, A.; Zaidi, S.J.; Mohsen, M.; Hawari, A.; Millar, G.J. Pressure retarded osmosis: Advancement, challenges and potential. *J. Water Process Eng.* **2021**, *40*, 101950. [[CrossRef](#)]
84. Cath, T.Y.; Elimelech, M.; Mccutcheon, J.R.; McGinnis, R.L.; Achilli, A. Standard methodology for evaluating membrane performance in osmotically driven membrane processes. *Desalination* **2013**, *312*, 31–38. [[CrossRef](#)]
85. Zimmerer, C.; Kottke, V. Effects of spacer geometry on pressure drop, mass transfer, mixing behavior, and residence time distribution. *Desalination* **1996**, *104*, 129–134. [[CrossRef](#)]
86. Schock, G.; Miquel, A. Mass transfer and pressure loss in spiral wound modules. *Desalination* **1987**, *64*, 339–352. [[CrossRef](#)]
87. Da Costa, A.R.; Fane, A.G. Net-Type Spacers: Effect of Configuration on Fluid Flow Path and Ultrafiltration Flux. *Ind. Eng. Chem. Res.* **1994**, *33*, 1845–1851. [[CrossRef](#)]
88. Haidari, A.; Heijman, S.; van der Meer, W. Visualization of hydraulic conditions inside the feed channel of Reverse Osmosis: A practical comparison of velocity between empty and spacer-filled channel. *Water Res.* **2016**, *106*, 232–241. [[CrossRef](#)]
89. Kavianipour, O.; Ingram, G.D.; Vuthaluru, H.B. Investigation into the effectiveness of feed spacer configurations for reverse osmosis membrane modules using Computational Fluid Dynamics. *J. Membr. Sci.* **2017**, *526*, 156–171. [[CrossRef](#)]
90. Abdelkader, B.A.; Sharqawy, M.H. Pressure drop across membrane spacer-filled channels using porous media characteristics and computational fluid dynamics simulation. *Desalin. Water Treat.* **2022**, *247*, 28–39. [[CrossRef](#)]
91. Ruiz-García, A.; De la Nuez, I. Feed Spacer Geometries and Permeability Coefficients. Effect on the Performance in BWRO Spiral-Wound Membrane Modules. *Water* **2019**, *11*, 152. [[CrossRef](#)]
92. Haidari, A.H.; Heijman, S.G.J.; van der Meer, W.G.J. Optimal design of spacers in reverse osmosis. *Sep. Purif. Technol.* **2018**, *192*, 441–456. [[CrossRef](#)]
93. Da Costa, A.; Fane, A.; Fell, C.; Franken, A. Optimal channel spacer design for ultrafiltration. *J. Membr. Sci.* **1991**, *62*, 275–291. [[CrossRef](#)]
94. Thomas, D.G. Forced Convection Mass Transfer in Hyperfiltration at High Fluxes. *Ind. Eng. Chem. Fundam.* **1973**, *12*, 396–405. [[CrossRef](#)]
95. Schwinge, J.; Wiley, D.E.; Fletcher, D.F. Simulation of the Flow around Spacer Filaments between Channel Walls. 2. Mass-Transfer Enhancement. *Ind. Eng. Chem. Res.* **2002**, *41*, 4879–4888. [[CrossRef](#)]
96. Kerdi, S.; Qamar, A.; Vrouwenvelder, J.S.; Ghaffour, N. Fouling resilient perforated feed spacers for membrane filtration. *Water Res.* **2018**, *140*, 211–219. [[CrossRef](#)]

97. Schwinge, J.; Neal, P.R.; Wiley, D.E.; Fletcher, D.F.; Fane, A.G. Spiral wound modules and spacers: Review and analysis. *J. Membr. Sci.* **2004**, *242*, 129–153. [[CrossRef](#)]
98. Fárková, J. The pressure drop in membrane module with spacers. *J. Membr. Sci.* **1991**, *64*, 103–111. [[CrossRef](#)]
99. Da Costa, A.R.; Fane, A.G.; Wiley, D.E. Spacer characterization and pressure drop modeling in spacer-filled channels.pdf. *J. Membr. Sci.* **1994**, *87*, 79–98. [[CrossRef](#)]
100. Sagiv, A.; Xu, W.; Christofides, P.D.; Cohen, Y.; Semiat, R. Evaluation of osmotic energy extraction via FEM modeling and exploration of PRO operational parameter space. *Desalination* **2016**, *401*, 120–133. [[CrossRef](#)]
101. Maisonneuve, J.; Pillay, P.; Laflamme, C.B. Pressure-retarded osmotic power system model considering non-ideal effects. *Renew. Energy* **2015**, *75*, 416–424. [[CrossRef](#)]
102. Roy, Y.; Sharqawy, M.H.; Lienhard, J.H. Modeling of flat-sheet and spiral-wound nanofiltration configurations and its application in seawater nanofiltration. *J. Membr. Sci.* **2015**, *493*, 360–372. [[CrossRef](#)]
103. Koutsou, C.; Yiantsios, S.; Karabelas, A. A numerical and experimental study of mass transfer in spacer-filled channels: Effects of spacer geometrical characteristics and Schmidt number. *J. Membr. Sci.* **2009**, *326*, 234–251. [[CrossRef](#)]
104. Geraldés, V. Flow management in nanofiltration spiral wound modules with ladder-type spacers. *J. Membr. Sci.* **2002**, *203*, 87–102. [[CrossRef](#)]
105. Gu, B.; Adjiman, C.S.; Xu, X.Y. The effect of feed spacer geometry on membrane performance and concentration polarisation based on 3D CFD simulations. *J. Membr. Sci.* **2017**, *527*, 78–91. [[CrossRef](#)]
106. Santos, J.; Geraldés, V.; Velizarov, S.; Crespo, J. Investigation of flow patterns and mass transfer in membrane module channels filled with flow-aligned spacers using computational fluid dynamics (CFD). *J. Membr. Sci.* **2007**, *305*, 103–117. [[CrossRef](#)]
107. Fimbres-Weihs, G.; Wiley, D. Review of 3D CFD modeling of flow and mass transfer in narrow spacer-filled channels in membrane modules. *Chem. Eng. Process. Process Intensif.* **2010**, *49*, 759–781. [[CrossRef](#)]
108. Koutsou, C.P.; Karabelas, A.J. Shear stresses and mass transfer at the base of a stirred filtration cell and corresponding conditions in narrow channels with spacers. *J. Membr. Sci.* **2012**, *399–400*, 60–72. [[CrossRef](#)]
109. Shakaib, M.; Hasani, S.; Mahmood, M. CFD modeling for flow and mass transfer in spacer-obstructed membrane feed channels. *J. Membr. Sci.* **2009**, *326*, 270–284. [[CrossRef](#)]
110. Toh, K.; Liang, Y.; Lau, W.; Fletcher, D. CFD study of the effect of perforated spacer on pressure loss and mass transfer in spacer-filled membrane channels. *Chem. Eng. Sci.* **2020**, *222*, 115704. [[CrossRef](#)]
111. Fimbres-Weihs, G.; Wiley, D. Numerical study of two-dimensional multi-layer spacer designs for minimum drag and maximum mass transfer. *J. Membr. Sci.* **2008**, *325*, 809–822. [[CrossRef](#)]
112. Landslide damage to the Boar River water supply pipeline, Bromley Hill, Jamaica: Case study of a landslide caused by Hurricane Gilbert (1988): Ahmad, R.; Earle, A.H.; Hugues, P.; Maharaj, R.; Robinson, E. *Int Assoc Engng Geol Bull* **1993**, *47*, April 1993, P59–70. *Int. J. Rock Mech. Min. Sci. Géoméch. Abstr.* **1994**, *31*, A46. [[CrossRef](#)]
113. Wardeh, S.; Morvan, H. CFD simulations of flow and concentration polarization in spacer-filled channels for application to water desalination. *Chem. Eng. Res. Des.* **2008**, *86*, 1107–1116. [[CrossRef](#)]
114. Schwinge, J.; Wiley, D.; Fletcher, D. A CFD study of unsteady flow in narrow spacer-filled channels for spiral-wound membrane modules. *Desalination* **2002**, *146*, 195–201. [[CrossRef](#)]
115. Ahmad, A.; Lau, K.K.; Abu Bakar, M. Impact of different spacer filament geometries on concentration polarization control in narrow membrane channel. *J. Membr. Sci.* **2005**, *262*, 138–152. [[CrossRef](#)]
116. Ranade, V.V.; Kumar, A. Fluid dynamics of spacer filled rectangular and curvilinear channels. *J. Membr. Sci.* **2006**, *271*, 1–15. [[CrossRef](#)]
117. Saeed, A.; Vuthaluru, R.; Yang, Y.; Vuthaluru, H.B. Effect of feed spacer arrangement on flow dynamics through spacer filled membranes. *Desalination* **2012**, *285*, 163–169. [[CrossRef](#)]
118. Picioreanu, C.; Vrouwenvelder, J.; van Loosdrecht, M. Three-dimensional modeling of biofouling and fluid dynamics in feed spacer channels of membrane devices. *J. Membr. Sci.* **2009**, *345*, 340–354. [[CrossRef](#)]
119. Li, Y.-L.; Tung, K.-L. CFD simulation of fluid flow through spacer-filled membrane module: Selecting suitable cell types for periodic boundary conditions. *Desalination* **2008**, *233*, 351–358. [[CrossRef](#)]
120. Li, Y.-L.; Tung, K.-L.; Lu, M.-Y.; Huang, S.-H. Mitigating the curvature effect of the spacer-filled channel in a spiral-wound membrane module. *J. Membr. Sci.* **2009**, *329*, 106–118. [[CrossRef](#)]
121. Vrouwenvelder, J.S.; Picioreanu, C.; Kruijthof, J.C.; Van Loosdrecht, M.C.M. Biofouling in spiral wound membrane systems: Three-dimensional CFD model based evaluation of experimental data. *J. Membr. Sci.* **2010**, *346*, 71–85. [[CrossRef](#)]
122. Karabelas, A.J.; Koutsou, C.P.; Sioutopoulos, D.C. Comprehensive performance assessment of spacers in spiral-wound membrane modules accounting for compressibility effects. *J. Membr. Sci.* **2018**, *549*, 602–615. [[CrossRef](#)]
123. Jeon, J.; Jung, J.; Lee, S.; Choi, J.Y.; Kim, S. A simple modeling approach for a forward osmosis system with a spiral wound module. *Desalination* **2018**, *433*, 120–131. [[CrossRef](#)]
124. Touati, K.; Tadeo, F.; Hänel, C.; Schiestel, T. Effect of the operating temperature on hydrodynamics and membrane parameters in pressure retarded osmosis. *Desalin. Water Treat.* **2015**, *57*, 10477–10489. [[CrossRef](#)]

125. Wang, Q.; Zhou, Z.; Li, J.; Tang, Q.; Hu, Y. Investigation of the reduced specific energy consumption of the RO-PRO hybrid system based on temperature-enhanced pressure retarded osmosis. *J. Membr. Sci.* **2019**, *581*, 439–452. [[CrossRef](#)]
126. Sivertsen, E.; Holt, T.; Thelin, W.R. Concentration and Temperature Effects on Water and Salt Permeabilities in Osmosis and Implications in Pressure-Retarded Osmosis. *Membranes* **2018**, *8*, 39. [[CrossRef](#)]
127. Touati, K.; Tadeo, F.; Schiestel, T. Impact of Temperature on Power Recovery in Osmotic Power Production by Pressure Retarded Osmosis. *Energy Procedia* **2014**, *50*, 960–969. [[CrossRef](#)]